JOURNAL OF SPACECRAFT AND ROCKETS
Vol. 44, No. 4, July–August 2007

Time-Resolved *I*-Band Photometry of Calibration Spheres and NaK Droplets

Doyle T. Hall,* John L. Africano,† and John V. Lambert‡
The Boeing Company, Colorado Springs, Colorado, 80919
and
Paul W. Kervin§
U.S. Air Force Research Laboratory, Kihei, Hawaii, 96753

DOI: 10.2514/1.27464

We have developed a program to obtain photometry of Earth-orbiting satellites using the U.S. Air Force advanced electrooptical system 3.6 m telescope's Visible Imager instrument, which acquires time-series charge-coupled device images at typical rates of 0.1 to 2.1 Hz. Observations of 12 spherical satellites provide measurements of *I*-band albedos (i.e., reflectances) and evaluation of surface nonuniformities. Best-fit specular + diffuse albedo models enable brightness predictions and a means to grade the quality of the spheres as photometric calibration reference objects. CalSphere-4A appears to be the highest quality calibrator of the 12, with the best-fit model reproducing 90% of the measurements to within ±0.03 stellar magnitudes. This four-decade-old sphere reflects in a predominantly diffuse fashion and has a total albedo of ≈67% that is somewhat lower than expected for fresh white paint, effects likely due to space weathering. The aluminum Lincoln Calibration Sphere-1 shows predominantly specular reflection (albedos ≈59%) but with ±0.3 magnitude deviations between data and model that recur every 30–90 s, likely due to one or more surface irregularities. Three other predominantly specular aluminum spheres display less frequent but larger amplitude deviations. Observations indicate that sodium/potassium droplets leaked from Soviet radar ocean reconnaissance satellite reactors are highly reflective specular spheres that can also serve as optical calibrators.

Nomenclature

A_D	=	albedo for Lambertian diffuse reflection from sphere
A_S	=	albedo for specular reflection from sphere
D	=	diameter of reflective sphere
$F_{M,j}$	=	model flux for measurement number j
$F_{S,j}$	=	incident solar flux for measurement number j
$f(\phi)$	=	Lambertian phase function for diffuse reflection from sphere
$I_{C,j}$	=	calibrated I-band stellar magnitude for Landolt standard star measurement number j
I_j	=	measured I-band stellar magnitude for measurement number j
$I_{M,j}$	=	model I-band magnitude flux for measurement number j
$I_{\max}$	=	maximum observed I-band magnitude for a satellite
$I_{\min}$	=	minimum observed I-band magnitude for a satellite
I_S	=	solar I-band magnitude at 1 AU solar range
$I_{S,j}$	=	solar I-band magnitude for measurement number j
i_j	=	instrumental magnitude for measurement number j
K	=	atmospheric extinction coefficient
N_F	=	no. of CCD frames used for albedo model analysis
N_P	=	no. of satellite passes used for albedo model analysis
$R_{C,j}$	=	calibrated R-band stellar magnitude for Landolt standard star measurement number j
$R_{O,j}$	=	satellite-to-observer range for measurement number j
$R_{S,j}$	=	satellite-to-sun range for measurement number j measured in AU
r_j	=	ratio of reflected flux to incident flux for measurement number j
$r_{M,j}$	=	model of ratio of reflected flux to incident flux for measurement number j
S_j	=	measured signal for observation j
X_j	=	atmospheric air mass for observation j
Z	=	instrumental photometric zero point
ΔI_j	=	uncertainty on I-band stellar magnitude for measurement number j
$\Delta I_{\max}$	=	I-band magnitude interval spanned by all observations of a satellite
ΔI_{90}	=	I-band magnitude interval spanned by the central 90% observations of a satellite
Δr_j	=	uncertainty on ratio of reflected flux to incident flux for measurement number j
ε	=	transformation coefficient for converting VisIm I-band magnitudes into Landolt I-band magnitudes
ϕ_j	=	phase angle, that is, sun–satellite–observer angle for measurement number j
χ_A	=	least-squares function for determining sphere albedos
χ_C	=	least-squares function for determining photometric calibration coefficients

Received 23 August 2006; revision received 9 February 2007; accepted for publication 12 February 2007.

*Engineer/Scientist 5, 5555 Tech Center Drive, Suite 400, Mail Code 846-R01F.

†Manager, 5555 Tech Center Drive, Suite 400, Mail Code 846-R01F (deceased).

‡Senior Scientist, 5555 Tech Center Drive, Suite 400, Mail Code 846-R01F. Professional Member AIAA.

§AMOS Technical Director, Directed Energy Directorate, DET15, 535 Lipoa Parkway, Suite 200.

I. Introduction

THE U.S. Air Force Maui Optical and Supercomputing (AMOS) site on Mount Haleakala, Maui, uses an assortment of telescopic optical systems to observe artificial Earth satellites. Several of these measure angular coordinates of satellites traversing the sky above Maui and contribute astrometric data to the larger U.S. Air Force effort to maintain an accurate and up-to-date catalog of orbiting objects. Other AMOS telescopic instrumentation is devoted to characterizing the physical properties of satellites, such as size, shape, orientation, reflectance, surface composition, etc. For

sufficiently large and bright satellites, the AMOS 3.6 m advanced electrooptical system (AEOS) telescope accomplishes much of this characterization mission through adaptive optics (AO) compensated imagery [1–3]. For instance, the AEOS imaging system easily resolves satellites such as the Hubble Space Telescope or the International Space Station, revealing surprising detail. However, many artificial satellites are either too dim or too distant to be imaged by the AEOS telescope. For instance, AEOS cannot resolve most operational satellites placed in distant geosynchronous orbit. Furthermore, many of the latest "micro" and "nano" satellites are simply too small to be resolved by AEOS or any other ground-based optical or radar facility, even though most occupy relatively low-altitude orbits. These nonresolvable objects must be characterized using nonimaging observational techniques. To help accomplish this task, AMOS has recently developed an observational program to use the AEOS telescope in its nonimaging mode to obtain calibrated time-resolved photometry of artificial satellites. This paper describes the AEOS photometry program including observation, data reduction, and calibration procedures and also reports measured reflectance properties for several spherical Earth-orbiting satellites.

II. Observational Instrumentation and Data Acquisition

All data presented in this paper were acquired using the AMOS AEOS 3.6 m telescope Visible Imager (VisIm) instrument [1–3]. The VisIm camera is the main scoring and science camera for the AEOS telescope employing a silicon-based 512×512 pixel cooled Pentamax EEV frame-transfer charged-coupled device (CCD) array receiving light in the 700–1050 nm wavelength range. The instrument has three fields of view: the narrow FOV (measuring 10×10 arc-s), the medium FOV (26×26 arc-s), and the wide FOV (62×62 arc-s). The VisIm system employs two eight-position filter wheels: one for spectral band filters and another for neutral density filters. The Pentamax EEV CCD dark current is $22e^-$/pixel/s at a temperature of $-40°$C, and the read noise is $12e^-$ rms. The camera output is digitized to 12 bits, with $10e^-$ per digital data number (DN). The 12-bit data readout digitally saturates at signals larger than 4095 DN/pixel/exposure, limiting the instrument's dynamic range but allowing for very fast data readout times. The maximum frame rate is slightly greater than 4 Hz and exposure times can be set as short as 10 ms.

Because nonresolvable satellites are generally too faint to allow fully compensated AO observations, the photometric observations typically employ only the VisIm tip-tilt image stabilization mode or no stabilization at all. To date, all AEOS photometric observations have employed the 62×62 arc-s VisIm wide FOV. Although the VisIm instrument is equipped with several spectral bandpass filters, all observations for this study employ the Bessel I-band filter.

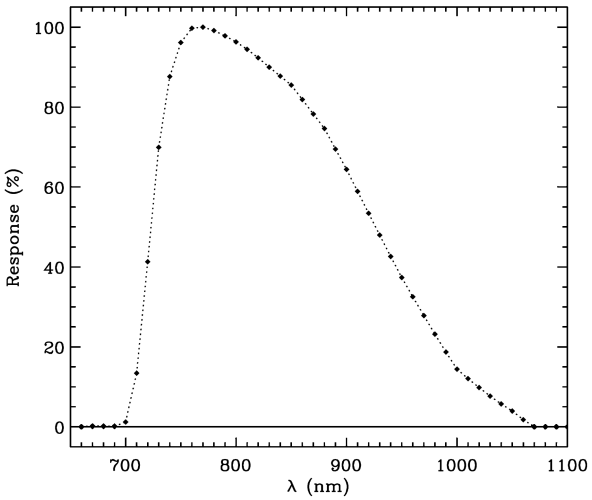

Fig. 1 Normalized response function for the AEOS VisIm instrument with the Bessel I-band filter.

Figure 1 shows the combined spectral response function for the VisIm/Bessel-I operating mode, indicating a peak response near 770 nm and full width at half-maximum spanning 725–925 nm. The Bessel I-band is similar to the standard astronomical Johnson filter I-band, so observing using this filter provides the means of establishing an accurate instrument calibration by observing photometric standard stars cataloged by Landolt [4]. The photometric observations also periodically employ one of three well-characterized neutral density filters, which provide the means to attenuate the signal from very bright sources to prevent signal saturation.

High-quality AEOS photometric observations require a sequence of well-exposed but unsaturated VisIm images of each target of interest, bracketed by observations of multiple calibration stars. Although the VisIm instrument is capable of exposures as short as 10 ms, observations shorter than approximately 250 ms suffer from an uncharacterized photometric nonlinearity. In practice, VisIm photometric exposure times vary depending on target brightness, but are generally 0.25–10.0 s in duration with each exposure requiring an additional 0.26 s overhead time. A time-series sequence of AEOS VisIm CCD images therefore provides "time-resolved" photometric measurements with typical data acquisition rates in the 0.1–2.1 Hz range. The photometric detection threshold for 1 s CCD exposure times is approximately 15th stellar magnitudes, but fainter targets have been detected with longer exposure times.

III. Photometric Data Reduction

One of the long-term goals for the AMOS photometric study of nonresolvable objects is that the data reduction procedures be as automated and self-contained as possible; that is, a "turn-key" operation, where nightly observations are processed using an automated procedure, and distilled data products are ready for inspection the next day. To address this goal, we have developed a VisIm photometry data reduction computer program called AOphot. Program AOphot is written in the interactive data language (IDL) and has been designed for easy use and the production of high-level data products that quickly summarize the results of observations.

To start the data reduction process, the raw data files that are automatically produced by the VisIm instrument must be converted to the flexible image transport system (FITS) image format [5,6]. Next, all of the FITS image files acquired during an observation shift must be stored into one single computer file system subdirectory. Any required auxiliary flat-field, bias, and dark images required for the CCD data reduction may either be put into that same directory or stored in standard library directories reserved for such instrumental calibration data. When all FITS files are in place, program AOphot may be executed. It performs all subsequent data reduction processing, including compiling an inventory of any targets observed during the observation shift, identifying the standard calibration stars and deriving the corresponding calibration coefficients, and, finally, producing several high-level data products designed to allow easy evaluation of each observed moving target. To facilitate the creation of quick-look data products, the multiple steps of this reduction process have been incorporated into a single data reduction script designed to be run by the AEOS telescope operators at the end of each observation shift; this script copies the raw data frames to a single subdirectory on a UNIX server computer devoted to photometric data reduction, converts the images to FITS format, and executes the AOphot reduction code on the server computer.

A. VisIm CCD Calibration—Bias, Dark, and Flat-Field Frames

The initial processing of VisIm images incorporates three steps common to most modern CCD systems [7]: 1) subtracting a CCD bias count image, 2) subtracting a CCD dark-count image scaled to the appropriate exposure time, and 3) dividing by a flat-field image. After these three processing steps, any residual signal remaining in the processed image may be attributed to photons incident on the CCD. VisIm bias, dark, and flat-field image frames are typically gathered once or twice per week, and stored for later use. When

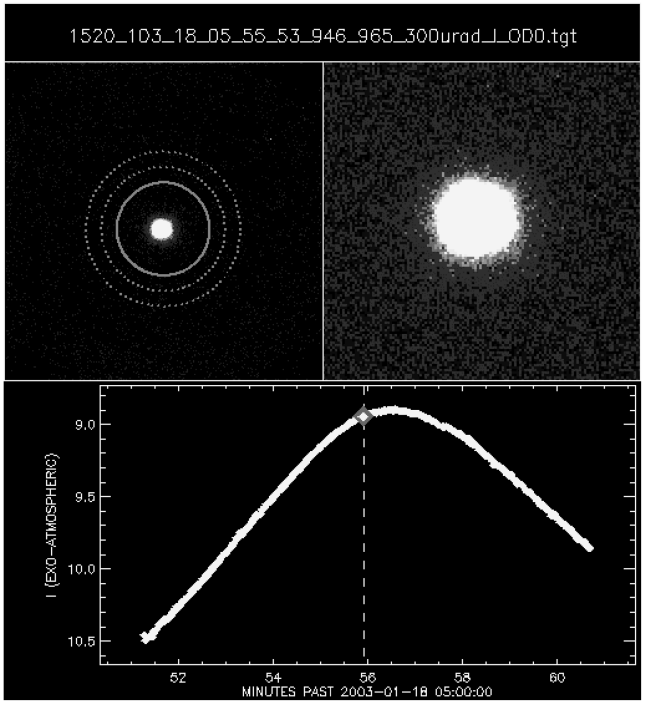

Fig. 2 Illustration of program AOphot screen display of a VisIm observation of SSN 01520. The text at the top shows the image file name. The upper left panel shows the 512 × 512 CCD image with superimposed representations of the circular photometry aperture (solid line) and sky annulus (dotted lines). The upper-right panel shows a zoomed-in view of the unresolved target. The lower panel shows a plot of the calibrated *I*-band magnitudes as a function of time.

processing AO-compensated imagery of resolved objects using the VisIm narrow FOV, these three steps are of critical importance to obtain the highest quality images possible. When processing non-AO photometric data taken with the VisIm 62 × 62 arc-s wide FOV, these processing steps typically yield an image featuring an unresolved "seeing blob" superimposed on a relatively constant sky-background signal (see Fig. 2). The total signal above the background can then be extracted using the aperture photometry technique described in the next section.

B. DAOPHOT Aperture Photometry

The VisIm photometry data reduction software program AOphot employs the DAOPHOT aperture photometry algorithm [8] to extract net target signals from the CCD images. Figure 2 shows an illustration of an aperture photometry extraction for a single VisIm data frame. The AOphot reduction program assumes that the brightest extended source of signal on the detector is that of the target of interest, and automatically centers a circular photometry aperture on the brightest source. An additional procedure determines if either the photometry aperture or the sky annulus is contaminated by star streaks and/or cosmic ray streaks. Given a sequence of images on a particular target, program AOphot extracts a signal for each image and tabulates a list of exposure midpoint times, net target signals, and associated signal uncertainties.

We have found that accurate photometric signals may be extracted from VisIm wide-FOV images by using a circular photometry aperture 9 arc-s in radius, which is large enough to include the entire source spread function, even for nearly saturated or slightly wind-jittered images. If strong winds buffet the AEOS telescope, the target can drift significantly on the CCD during an exposure and the effective source spread function can be enlarged significantly. The photometry aperture and sky annulus shown in the upper left panel of Fig. 2 as the solid and dotted circles, measure 9, 12, and 15 arc-s in radius, respectively, which are the default sizes for program AOphot. However, these radii may be adjusted as required for badly wind-jittered images.

C. Bad-Frame Detection

To collect VisIm photometric observations on artificial Earth satellites, the AEOS telescope must track and follow the objects as they traverse the sky above the observatory. If successful, this keeps the targeted satellite stationary near the center of the VisIm wide FOV, creating a compact, sharply peaked source signature like that shown in the upper panels of Fig. 2. The tracked object will occasionally pass near bright stars, and these appear as streaks across the detector. If such a star streak passes within the region defined by the photometry aperture or sky annulus, the DAOPHOT extraction process could yield an inaccurate measure of the net target signal depending on the relative brightness of the star and target satellite. During the automated reduction process, program AOphot identifies and rejects such "bad frames" by determining if any statistically significant signals (i.e., those exceeding the sky-background level by 5 standard deviations) traverse the aperture and/or sky annulus. However, the tracking may be poor due to several reasons, including an inaccurate satellite ephemeris data, or strong winds buffeting the AEOS telescope. In these cases, the target may drift within the wide FOV and the AEOS telescope operators must adjust the pointing midexposure. These midexposure corrections can lead to an extended source of signal on the CCD, sometimes resulting in two bright spots or sometimes a signal distribution shaped like a "dumbbell." In these cases, program AOphot will reject the frame as bad if any statistically significant portion of this extended source signal distribution traverses the aperture and/or sky annulus.

D. Quick-Look Reduction for VisIm Wide-FOV Observations

The VisIm wide-FOV flat-field image is relatively constant over the central portion of the CCD; within about 200 pixels of the center of the 512 × 512 pixel array, flat-field image variations are less than ≈10%. Furthermore, both the bias and dark-count images are also relatively flat over this central region of the CCD. Because of this, we have found that applying the aperture photometry technique directly to raw CCD data provides an efficient means of extracting "quick-look" photometry, without having to account for CCD bias, dark-count, and flat-field effects. In other words, quick-look photometry reductions skip the bias, dark-count, and flat-field corrections and proceed directly to the aperture photometry step. Applying the aperture photometry procedure to fully debiased, dark-subtracted, and flat-fielded images yields the most accurate, "fully processed" photometric measurements. Comparisons between fully processed data and quick-look data indicate that the two methods produce photometric measurements that are generally within 5% of one another.

The reason that the quick-look procedure works to an accuracy of ≈5% is because the flat-field variations for the VisIm wide FOV are relatively small over a large central region of the detector. As explained in more detail below, when a DAOPHOT photometry aperture and sky annulus are used to extract the net signal above background, the signal measured within the sky annulus is used to estimate the background signal underlying those pixels within the photometry aperture. In the quick-look reduction method, if both photometry aperture and sky annulus are restricted to the central flat-response region of the detector, then the sky annulus provides a reasonably accurate estimate of all nontarget signals *including sky-background, bias, and instrumental dark counts*. In the fully processed reduction method, the sky annulus provides a measure of only sky-background counts. In cases where flat-field variations across the detector are relatively large, such as in the VisIm narrow FOV, this quick-look procedure would not be appropriate because it would yield much less accurate results.

E. Photometric Calibration Procedure

AEOS VisIm observations of standard photometric stars provide the means to derive the calibration coefficients required to convert

raw VisIm photometric signals into stellar magnitudes. Ideally, calibration star observations should be intermixed with targeted-object data throughout an observation shift, with the goal of providing good coverage of air mass as well as calibration star magnitude and color. Multiple calibration stars (i.e., ≥ 10) are typically observed throughout each observation shift, and during each calibration star observation, roughly 10–20 VisIm images are acquired. This technique of "all-sky" photometry seeks to characterize the atmospheric extinction coefficient throughout the entire observation shift by observing stars at multiple air-mass values. The calibration data also provide the means to measure the instrumental zero point, and subsequent absolute photometric calibration of the moving target data.

1. Landolt Photometric Standard Calibration Stars

Landolt [4] tabulated an extensive set of photometric standard stars, calibrated to an accuracy of 1–2% in the astronomical U, B, V, R, and I bands. Although the Landolt I-band spectral response is not exactly the same as the VisIm Bessel I-band shown in Fig. 1, a simple transformation allows an approximate cross calibration of the two. The Landolt photometric star catalog has been programmed into the AEOS telescope operator's console, easing the task of calibration star acquisition. This enables telescope operators to simply "dial in" the number assigned to a particular calibration star, and the telescope control system automatically retrieves the astrometric coordinates and slews the telescope appropriately, usually resulting in the requested star being very nearly centered in the VisIm wide FOV. Another advantage of this preprogrammed calibration star method is that the number assigned by the telescope control system to each calibration star then becomes associated with all CCD image data files associated with that star. The data reduction program AOphot then can use these numbers to automatically identify VisIm images of calibration stars, distinguishing them from files associated with any other objects observed during an observation shift.

2. Deriving Calibration Coefficients from Calibration Star Observations

After the calibration star identification procedure is complete, program AOphot extracts the calibration star signals using the DAOPHOT aperture photometry method, employing exactly the same photometry aperture and sky annulus radii used for all other targets. The program then uses the extracted signals to derive instrumental calibration coefficients. These calibration coefficients provide the means to convert raw VisIm signals into stellar magnitudes.

Extracted net signals (counts/second or DN/second) from each recorded image are denoted S_j, where j is an index spanning all calibration star images acquired during the observation shift. The instrumental magnitude i_j is a logarithmic measure of the total signal:

$$i_j = -2.5\log_{10}(S_j) \tag{1}$$

The I-band magnitude of the jth calibration star measurement I_j is related to the net signal as follows:

$$I_j = i_j + Z - KX_j + \varepsilon(R_{C,j} - I_{C,j}) \tag{2}$$

where Z is the *zero point*, K the *extinction coefficient*, and ε the *transformation coefficient*. In Eq. (2), X_j denotes the air mass of the measurement, $I_{C,j}$ the calibrated I-band magnitude for the photometric standard star (as tabulated by Landolt), and $R_{C,j}$ the calibrated R-band magnitude. The transformation coefficient ε has been introduced [9] to account for the difference between the VisIm Bessel I-filter spectral bandpass and the Johnson I-filter bandpass used by Landolt. Equations (1) and (2) provide a means of calculating the calibrated I-band magnitude from VisIm signals, which is often referred to as the "exoatmospheric" magnitude because the effects of atmospheric extinction have been removed.

To derive the three calibration coefficients Z, K, and ε defined in Eq. (2), at least three photometric measurements of calibration stars must be made. However, in practice, deriving well-defined values for Z, K, and ε requires 10–15 calibration star measurements, spanning a range of air masses X_j, absolute magnitudes $I_{C,j}$, and color differences $(R_{C,j} - I_{C,j})$. Program AOphot employs a least-squares analysis procedure [10] to find best-fit values for the three coefficients. Specifically, the program finds the minimum of the least-squares function

$$\chi^2_C(Z,\ K,\ \varepsilon) = \sum_j (I_j - I_{C,j})^2/\Delta I_j^2 \tag{3}$$

with respect to the three variables Z, K, and ε. In Eq. (3), ΔI_j denotes the statistical uncertainty of the measured instrumental magnitude I_j.

F. Expected Variations in Calibration Coefficients

Typically, observations of several calibration stars taken during a single telescopic observation shift are combined to determine calibration coefficients appropriate for that observation shift. Extinction coefficients are expected to vary, reflecting nightly changes in the I-band atmospheric transmission. However, because the zero point represents the overall sensitivity of the telescope + instrument system, best-fit zero points should not change rapidly unless the telescope optics or the VisIm instrument has been altered. For instance, on occasion the AEOS telescope primary and/or secondary mirrors are cleaned during routine maintenance. This cleaning activity typically increases the mirror reflectivity thereby increasing the overall sensitivity of the system. Similarly, as telescope optical elements degrade or become dirty over time, the zero point tends to decline slowly. The zero point should also tend to decline if the CCD detector array suffers sensitivity loss over its operational lifetime. The transformation coefficient ε that accounts for the difference between the AEOS VisIm bandpass and the

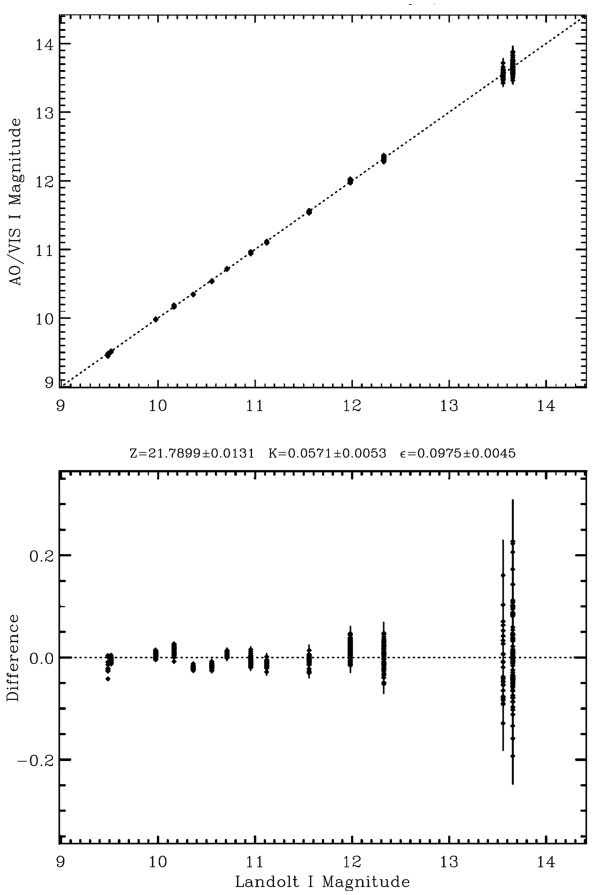

Fig. 3 Relationship between measured I-band magnitudes and the reference values tabulated by Landolt [4] for calibration stars observed on 18 January 2003. The top panel shows the measurements I_j on the y axis plotted against the calibrated I-band magnitude $I_{C,j}$ on the x axis. The bottom panel shows a plot of the differences $(I_j - I_{C,j})$.

bandpass used by Landolt [4] should not vary rapidly in time, unless the telescope + instrument spectral response has been significantly altered by maintenance or degradation.

G. Measured AEOS VisIm *I*-band Calibration Coefficients

Figure 3 shows the results of a typical least-squares calibration analysis for AEOS VisIm calibration stars observed on the 18th day of 2003 (2003-018) and reduced using the AOphot quick-look procedure. The top panel shows the VisIm measurements I_j on the y axis plotted against tabulated calibration star I-band magnitude $I_{C,j}$ on the x axis. The bottom panel shows a plot of the differences $(I_j - I_{C,j})$ against $I_{C,j}$. The least-squares analysis yields best-fit photometric calibration coefficients of $Z = 21.790$, $K = 0.057$, and $\varepsilon = 0.098$ for this night. Table 1 lists the calibration coefficients for the 18 nights when satellite observations were conducted for this analysis. Before any observations were conducted during each of these nights, visual inspection of the sky indicated that the observing conditions at the AEOS telescope were "photometric" (i.e., with no visible clouds and clear star visibility extending from zenith down to the horizon in all directions). Table 1 indicates some variability in the zero point of the instrument. Some of this variation is due to statistical measurement uncertainty, but some was also caused by changes in the AEOS + VisIm system optical elements. For instance, on 2003-033, observations were conducted without a dichroic beam-splitting element that is normally inserted into the optical path, leading to an increased sensitivity of about 0.13 magnitudes over the previous tabulated night. Similarly, between 2003-076 and 2004-013, the AEOS mirror was cleaned as a part of normal maintenance activity. The average zero point for the 13 tabulated nights preceding this cleaning was $Z = 21.77 \pm 0.08$, whereas the average for the five nights afterwards was $Z = 22.04 \pm 0.02$, indicating that the cleaning process produced an overall system sensitivity increase of about 0.27 magnitudes. Table 1 also indicates that for these 18 photometric nights the I-band atmospheric extinction coefficient varied from 0.027 up to 0.102 magnitudes per air mass, with an average value of $K = 0.053 \pm 0.024$. Best-fit transformation coefficients measured during the same nights varied between 0.074 and 0.138, with an average value of $\varepsilon = 0.11 \pm 0.02$.

As can be seen in Fig. 3, during reasonable photometric seeing conditions residual differences between measured and known I-band magnitudes $(I_j - I_{C,j})$ are generally ≤ 0.05 magnitudes for targets brighter than 12.5 magnitudes. On the best photometric nights these residuals can be $\approx$0.02, indicating that the AEOS VisIm system is capable of photometric accuracies in the range of 2–5%.

H. Photometric Calibration of Objects Reflecting Sunlight

Reflected sunlight dominates the I-band brightness of Earth satellites as well as most other solar system bodies. Equation (2) can be used to derive the calibrated magnitudes for these objects, but requires an estimate for the R–I color of the object. Unfortunately, the VisIm system does not include an R-band filter, preventing a direct measurement of this color term. In this analysis we approximate the R–I color of all sunlight-reflecting objects to be equal to 0.34 magnitudes, which is the R–I color of the sun itself [11]. This approximation neglects any difference in object reflectance between the photometric R-band (peak $\approx$700 nm) and the VisIm I-band (peak $\approx$ 770 nm). Analysis of spectral data indicates that the R- and I-band albedos for artificial Earth satellites are often very nearly the same and are generally within $\approx$30% of one another [12], implying that this approximation results in an error of less than $\approx$0.04 magnitudes.

Table 1 VisIm calibration coefficients for dates in which satellite observations were acquired

Date (year-day)	Z	K	ε	Observed SSN
2003-017	21.785	0.031	0.117	01361
2003-018	21.790	0.057	0.098	01361, 01520
2003-033	21.921	0.044	0.138	01361
2003-041	21.851	0.089	0.107	01361
2003-050	21.783	0.035	0.116	04168
2003-054	21.758	0.029	0.100	04168
2003-060	21.753	0.036	0.115	00900, 01361
2003-061	21.824	0.069	0.074	00900, 00902
2003-064	21.757	0.043	0.129	01361, 01520
2003-073	21.843	0.102	0.122	00900, 00902
2003-074	21.641	0.028	0.145	00900, 00902
2003-075	21.617	0.027	0.133	00902
2003-076	21.710	0.055	0.106	02909
2004-013	22.030	0.054	0.119	26505
2004-019	22.023	0.028	0.096	26521
2004-054	22.043	0.078	0.110	26512, 26534
2004-097	22.022	0.057	0.102	26506, 26512
2004-122	22.060	0.085	0.110	26516, 26634

IV. Spherical Satellite *I*-Band Albedo Measurements

Table 2 lists the spherical satellites analyzed in this work, including NORAD (North American Aerospace Defence Command) Space Surveillance Network (SSN) object numbers, international designators, common names, known diameters, and surface material characteristics. Each satellite was observed on one or more nights, as listed Table 1. During each observation, the AEOS telescope tracked the satellite during one traversal over the observatory (i.e., one "pass") recording multiple CCD frames per pass. Because the AEOS telescope does not normally operate during the daytime, the observed satellite passes necessarily occur just after sunset or just before sunrise. Only during such "terminator passes" are these low-Earth orbit satellites in sunlight at the same time that the observatory has sufficiently dark conditions to operate. Table 2 also lists the total number of passes (N_P) and CCD frames (N_F) combined to derive the best-fit I-band albedo values (A_S and A_D), the minimum ($I_{\min}$) and maximum ($I_{\max}$) exoatmospheric I-band magnitudes observed for each sphere, as well as two parameters that indicate how well the best-fit model reproduces the observed data for each sphere (ΔI_{90} and $\Delta I_{\max}$, described later in more detail).

Table 2 Observed spherical satellite properties and best-fit *I*-band albedos

SSN	Int. desig.	D, cm	Surface	N_P	N_F	$I_{\min}$	$I_{\max}$	A_S, %	A_D, %	ΔI_{90}	$\Delta I_{\max}$
00900	1964-063C	36.0	Aluminum	4	886	8.0	10.2	64.6	0.0	0.21	0.80
00902	1964-063E	36.0	Aluminum	4	1280	7.3	11.8	57.6	4.8	0.39	2.12
01361	1965-034C	113.0	Aluminum	6	1872	7.5	9.5	57.5	1.4	0.22	1.07
01520	1965-065H	36.0	White paint	2	599	8.5	10.7	1.5	65.3	0.03	0.07
02909	1967-053J	41.0	Aluminum	1	320	8.0	10.4	52.9	0.0	0.35	2.02
04168	1969-082H	41.0	Anodized aluminum	2	205	11.3	13.9	0.76	0.91	0.20	0.73
26505	1981-021G	5.6	NaK metal	1	130	12.4	13.5	90.6	0.0	0.12	0.26
26506	1981-021H	5.3	NaK metal	1	60	11.9	13.9	85.2	0.0	0.06	0.22
26512	1981-021P	5.7	NaK metal	2	154	11.8	13.6	86.3	0.0	0.06	0.12
26516	1984-069H	5.1	NaK metal	1	80	12.4	13.7	85.0	0.0	0.12	0.23
26521	1981-069N	4.9	NaK metal	1	197	12.5	14.0	99.3	0.0	0.12	0.33
26634	1981-069R	5.2	NaK metal	2	123	11.9	13.6	86.9	0.0	0.10	0.18

A. Theoretical Brightness of Reflective Spheres

A simple analytical model for the sunlight reflected from a uniform spherical satellite may be expressed by summing components due to diffuse and specular reflection. In terms of band-averaged flux, this *two-component reflectance model* may be written [13] as

$$F_{M,j} = F_{S,j}\left(\frac{D^2[A_S + A_D f(\phi_j)]}{16R_{O,j}^2}\right) \tag{4}$$

where $F_{M,j}$ denotes the band-averaged model flux for observation j, $F_{S,j}$ is the incident band-averaged solar flux, D the diameter of the sphere, A_S and A_D the sphere's band-averaged albedos (i.e., reflectances) for specular and diffuse reflection, and $R_{O,j}$ the observer-to-satellite range. The function $f(\phi)$ accounts for how the flux reflected from a Lambertian diffuse sphere depends on the sun–satellite–observer angle (or *phase* angle), ϕ, given by

$$f(\phi) = \left(\frac{8}{3\pi}\right)[\sin\phi + (\pi - \phi)\cos\phi] \tag{5}$$

B. Least-Squares Albedo Determination Method

Using a series of calibrated measurements of the I-band magnitude for a particular spherical satellite, best-fit specular and diffuse albedo components may be determined using a least-squares analysis procedure. The analysis employed here seeks a best-fit reproduction of the ratio of the reflected flux to the incident solar flux, which may be written in terms of the exoatmospheric I-band magnitude as follows:

$$r_j \equiv F_j/F_{S,j} = 10^{-0.4(I_j - I_{S,j})} \tag{6}$$

In Eq. (6) I_j denotes the jth measurement of the exoatmospheric magnitude and $I_{S,j}$ the solar magnitude given by

$$I_{S,j} = I_S + 5\log_{10}(R_{S,j}) \tag{7}$$

where $R_{S,j}$ is the sun-to-satellite range [measured in astronomical units (AU)] and $I_S = -27.63$ is the I-band magnitude of the sun at a solar range of 1 AU [11]. Equations (4) and (5) may be used to write a model expression for the ratio defined in Eq. (6):

$$r_{M,j} = \left(\frac{D^2[A_S + A_D f(\phi_j)]}{16R_{O,j}^2}\right) \tag{8}$$

Given the sphere diameter as well as the observation phase angles and ranges, best-fit values for the albedos A_S and A_D may be determined by minimizing a least-squares function of the form

$$\chi_A^2(A_S, A_D) = \sum_j (r_j - r_{M,j})^2/\Delta r_j^2 \tag{9}$$

where Δr_j is the measurement uncertainty of the ratio r_j. To determine physically plausible albedo values, the analysis employs a *bounded least-squares method* [10] subject to the following bounding constraints: $0 \le A_S \le 1$, $0 \le A_D \le 1$, and $0 \le A_S + A_D \le 1$. Saturated CCD frames are excluded from the analysis as well as observations with altitude angles (i.e., elevation angles) less than 15 deg to avoid biases associated with large air mass values.

C. Derived Albedos and the Quality of Best-Fit Models

Table 2 lists best-fit albedos for 12 spherical satellites analyzed in this work; the first four columns give the SSN number, the international designator, the diameter D, and the surface material for each satellite. Table 2 also lists the total number of satellite passes N_P and individual CCD frames N_F, combined to derive the best-fit albedos as well as the minimum and maximum I-band magnitudes in the combined data set, $I_{\min}$ and $I_{\max}$. The best-fit albedos listed in Table 2 provide a means of calculating a model I-band magnitude for each measurement using the following expression:

$$I_{M,j} = I_S - 2.5\log_{10}\left(\frac{D^2[A_S + A_D f(\phi_j)]}{16R_{O,j}^2 R_{S,j}^2}\right) \tag{10}$$

The quality of the fit can be judged by how accurately this model reproduces the observed magnitudes and quantitatively measured by the distribution of the residual differences $|I_j - I_{M,j}|$. The last two columns of Table 2 provide two such measures of the fit quality ΔI_{90} and $\Delta I_{\max}$. The first of these indicates the residual difference that includes 90% of the observations; in other words, $|I_j - I_{M,j}| \le \Delta I_{90}$ for 90% of the measurements. The second indicator $\Delta I_{\max}$ indicates the maximum residual difference $|I_j - I_{M,j}|$ for all observations.

The first six satellites listed in Table 2 are spheres launched specifically for the purposes of calibrating ground-based radar and/or optical systems and have known diameters and surface materials [14]. The last six are droplets of sodium–potassium metal leaked from Soviet radar ocean reconnaissance satellite (RORSAT) nuclear reactors [15–18]. These 12 satellites, their measured albedos, and their utility as I-band optical calibration objects will be discussed further in the following sections.

D. SSN 01520: A High-Quality Diffuse Calibrator

Calsphere-4A (1965-065H) was launched in August of 1965 and currently occupies a 1075 km × 1180 km × 90.2 deg orbit. It is a 0.36 m diam sphere made of aluminum and painted white before launch [14]. Data from two passes conducted on 2003 days 018 and 064 comprising 599 CCD frames were combined for the albedo determination analysis. Figure 4 shows the measured exoatmospheric and range-normalized magnitudes for the 2003-018 pass plotted along with the best-fit model, calculated using albedo values $A_S = 1.5\%$ and $A_D = 65.3\%$. The relatively small best-fit specular albedo indicates that SSN 01520 is nearly a purely diffuse reflecting sphere. The combined specular + diffuse albedo of ≈67% is somewhat lower than the ≈80% total albedo expected for fresh white paint. However, SSN 01520 has been on orbit for about four decades and this discrepancy suggests that the paint may have darkened in the I-band over time due to space weathering. The relatively small specular albedo component could also conceivably be due to weathering making the white paint more powdery and less shiny over time.

The best-fit model for SSN 01520 reproduces the observations within 0.03 magnitudes for 90% of the observations, with a maximum deviation of 0.07 magnitudes. These deviations between model and data are smaller than any of the other spheres studied in this analysis, making this the most accurate optical calibrator of the 12. SSN 01520 also has the advantage of being relatively bright (up to magnitude 8.5) making it relatively easy to detect. Unfortunately, the high inclination orbit of SSN 01520 means that it does not make terminator passes every day over most ground-based observatories.

E. SSN 01361: A Mostly Specular Sphere with Surface Irregularities

Lincoln Calibration Sphere-1 (1965-034C) was launched in May of 1965 and currently occupies a 2780 km × 2797 km × 32.1 deg orbit. It is a 1.13 m diam sphere made of unpainted aluminum [14]. Data from six passes (1872 CCD frames) were combined to derive best-fit albedos of $A_S = 57.5\%$ and $A_D = 1.4\%$. Figure 5 shows the calibrated magnitudes recorded during passes on 2003-018 and 2003-060, each plotted along with the best-fit model. The relatively small diffuse albedo indicates that SSN 01361 is mostly a specular reflector. The best-fit model reproduces the data to within 0.22 magnitudes for 90% of the measurements with a maximum deviation of 1.07 magnitudes. These residuals are caused by the existence of systematic deviations between data and model that significantly exceed the size of the measurement errors. Figure 5 shows that these deviations have amplitudes of about ±0.3 magnitudes and tend to recur on a time scale of roughly 30–90 s. These deviations are not associated with changes in target range or phase angle, and similar variations appear consistently in all VisIm observations of SSN 01361. Preliminary analysis suggests that these variations are

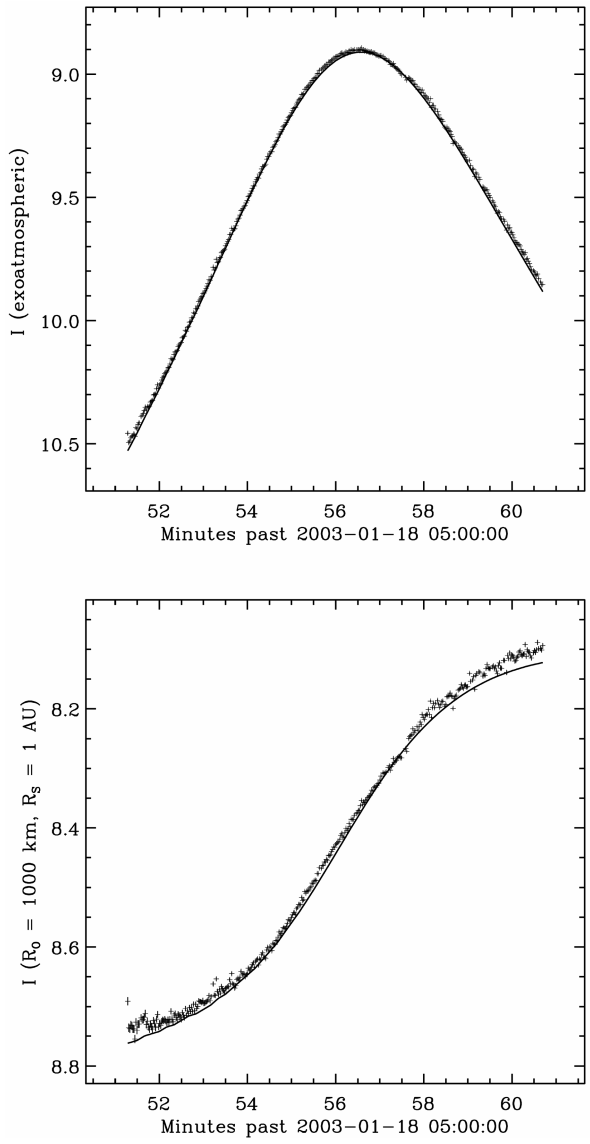

Fig. 4 ***I*-band magnitudes for SSN 01520 measured on 2003-018 (+) plotted with the best-fit model (solid line). The top panel shows the exoatmospheric magnitudes with peak brightness corresponding to the minimum observer-to-satellite range of $R_O = 1273$ km. The bottom panel shows the magnitudes adjusted to account for the $1/R^2$ variations in observer and solar range, normalized to values of $R_O = 1000$ km and $R_S = 1$ AU.**

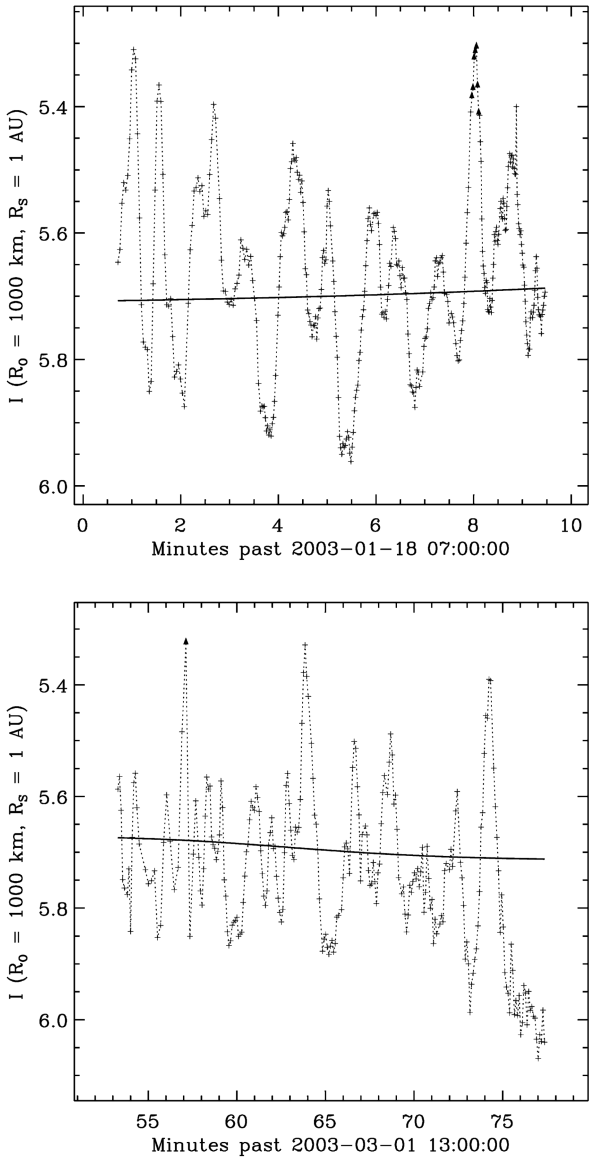

Fig. 5 Range-normalized *I*-band magnitudes for SSN 01361 (+ connected with dashed lines) plotted with the best-fit model (solid line). The top panel shows data from 2003-018 (JAN-18) and the bottom panel from 2003-060 (MAR-01). The points shown as upward-pointing triangles represent saturated measurements excluded from the best-fit analysis.

caused by irregularities on the surface of the sphere. If this were the case, then the 30–90 s recurrence time scale is likely associated with the rotation period of the satellite in some manner. The size of such irregularities would not have to be large to create an appreciable change in brightness, because the size of the reflected disk of the sun on the sphere is so small. For a perfectly specular sphere of diameter 1.13 m observed at a phase angle of zero, the reflected solar disk has the approximate shape of a circle on the surface of the sphere with 0.26 cm diameter. As the phase angle increases the reflected solar disk elongates into a nearly elliptical shape, but even at the largest phase angle in which SSN 01361 observations were conducted ($\phi = 130$ deg), the spot measures ≤ 0.62 cm. This means that irregularities with size scales ≤ 1 cm could change the brightness significantly. For instance, a "patchy" specular albedo pattern with isolated 1 cm regions where $A_S \leq 0.3$ could explain the ± 0.3 magnitude variations. Preliminary analysis also suggests that comparably small irregularities in the radius of curvature could account for the observed variations. For example, a local variation in the radius of curvature of +10 cm (i.e., a slight "flattening" of the surface) could produce the observed brightness variations, such as that due to a small impact crater or a manufacturing seam.

This phenomenon, whatever the cause, makes SSN 01361 a suitable optical calibrator only for observations that monitor the brightness over several of the deviations, or roughly 5 min. Observation periods much shorter than this do not provide enough of a baseline to average out the variations. However, the low inclination orbit of SSN 01361 means that it generally makes multiple terminator passes per day over many low- and midlatitude ground-based observatories. This, plus the fact that SSN 01361 is a relatively bright object (up to magnitude 7.5), generally provides ample opportunities to gather sufficient data to average over the observed variations.

F. SSN 00900, 00902, and 02909: Mostly Specular Spheres with Significant Irregularities

Calibration spheres SSN 00900, 00902, and 02909 are also predominantly specular reflectors, and each shows evidence of surface irregularities. To illustrate this, Fig. 6 shows calibrated

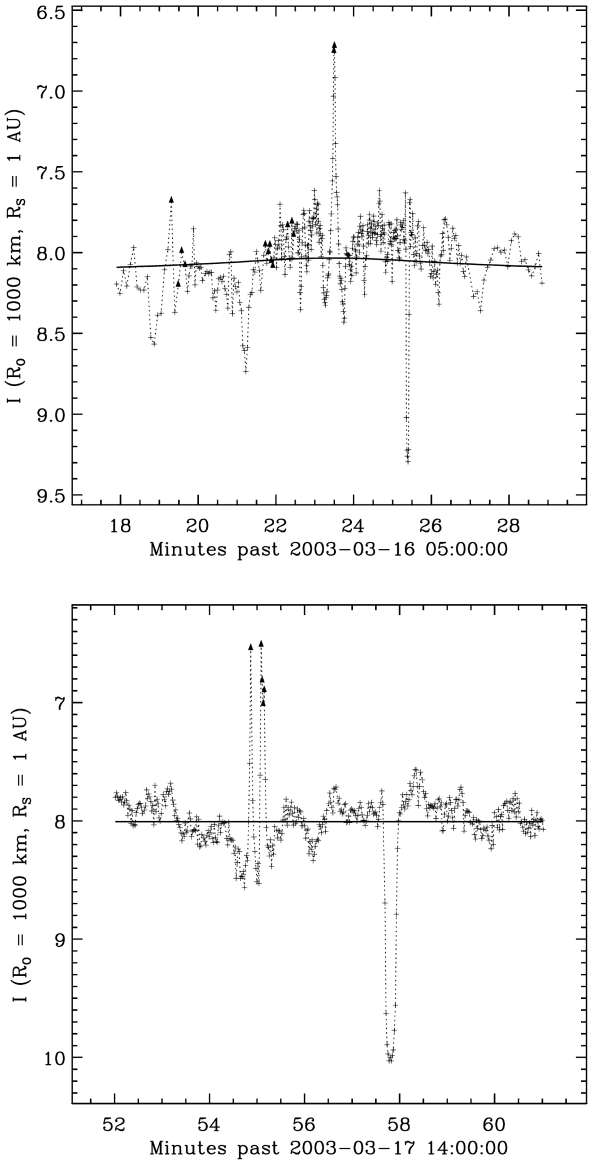

Fig. 6 Range-normalized *I*-band magnitudes for SSN 00902 (top panel) and SSN 02909 (bottom panel) measured on 2003-076 (+ connected with dashed lines) plotted with the best-fit models (solid lines). Two pronounced deviations between data and model appear in each panel suggesting the existence of surface irregularities.

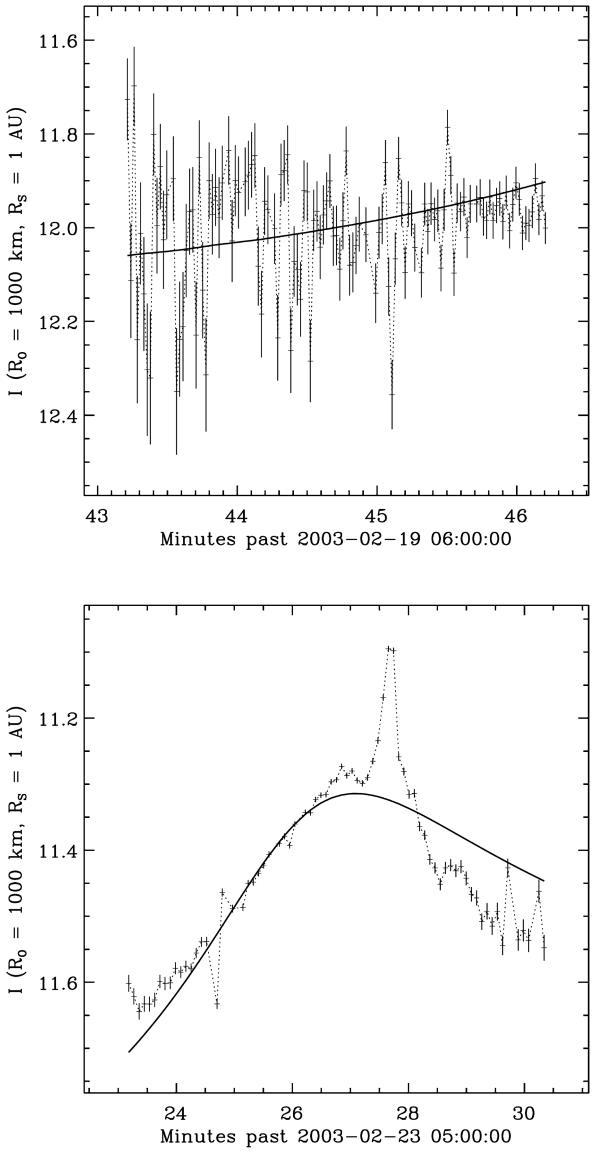

Fig. 7 Range-normalized *I*-band magnitudes for SSN 04168 (+ with error bars connected with dashed lines) and best-fit model (solid line). The pronounced deviation between data and model in the bottom panel (near 05:27:45 UT) suggests the existence of at least one surface irregularity on this calibration sphere.

magnitudes for SSN 00902 recorded on 2003-075 and SSN 02909 recorded 2003-076, each plotted along with the best-fit model. Two large-amplitude deviations between data and model are clearly apparent in each panel, and deviations of similar amplitude and form are observed in SSN 00900 as well. These deviations have distinctly different photometric signatures than those observed for SSN 01361. In particular, they have larger amplitudes of up to two magnitudes. Secondly, they do not recur on a characteristic time scale or in an easily identifiable temporal pattern. Preliminary analysis suggests that relatively small, localized variations in the radius of curvature on each of these predominantly specular spheres could explain both the shape and the amplitude of such deviations. Although more modeling is required for a definitive explanation, such surface irregularities could conceivably be caused by micrometeoroid or small debris impacts. The existence of these large-amplitude deviations makes SSN 00900, 00902, and 02909 suitable optical calibrators only for observations that provide sufficiently long observations to identify and account for these patterns. In other words, isolated short-duration observations for these spheres could potentially deviate significantly from the best-fit model.

G. SSN 04168: A Dark Sphere with at Least One Surface Irregularity

Tempsat-2 (1969-082H) was launched in September of 1969 and currently occupies a 900 km × 925 km × 70 deg orbit. It is a 0.41 m diam sphere with a black anodized aluminum surface [14]. Photometric observations from two passes yield best-fit albedos of $A_S = 0.76\%$ and $A_D = 0.91\%$. These very small albedos indicate that SSN 04168 is extremely nonreflective, consistent with its known anodized aluminum surface. Figure 7 shows the calibrated magnitudes recorded during passes on 2003-050 and 2003-054, each plotted along with the best-fit model. A statistically significant 0.2 magnitude upward deviation lasting ≈30 s apparent in the second pass suggests that this sphere possesses at least one surface irregularity.

H. NaK Metallic Droplet Debris: High-Quality Specular Calibrators

The last six spherical satellites studied here were not originally launched as calibration spheres, but are orbital debris resulting from the leakage of liquid sodium-potassium (NaK) coolant from RORSAT nuclear reactors [15–18]. The former Soviet Union launched approximately 30 RORSAT-class nuclear-powered ocean reconnaissance satellites from 1967 through 1988. Upon retirement,

these satellites ejected their fuel cores into high-altitude disposal orbits in an effort to prevent the radioactive material from reentering Earth's atmosphere for several hundred years. During or after these fuel core ejection events, faulty seals on several of the RORSAT reactor coolant systems allowed liquid metallic NaK reactor coolant to leak into space forming a population of "droplets" that comprise a significant fraction of the orbital debris population near 900 km altitude [15]. Many are large enough to be tracked and characterized by radar [18] and ground-based optical telescopes [16]. Theoretical analysis of the expected physical properties of these objects [17] indicate that, after leaking from the RORSAT satellites, the liquid metallic NaK reactor coolant should naturally form into highly reflective spherical droplets that will slowly evaporate in space as they orbit the Earth. A detailed analysis of multiple radar observations confirms that 26 of the largest droplets do indeed have a spherical or near-spherical shape and are a bit smaller than a tennis ball on average [18].

AEOS photometric observations of six NaK droplets indicate that the range-normalized I-band magnitudes of these objects remain constant as a function of time to within statistical uncertainty [19]. This implies that the range-normalized magnitudes are also constant as a function of solar phase angle as well. In other words, these objects all display "flat phase curves" to within measurement error, as illustrated in Fig. 8 for two of the NaK droplet observations. Equation (10) indicates that this phenomenon is expected for spheres that reflect sunlight in a purely specular fashion. A combined least-squares analysis of all of the AEOS NaK observations indicates that diffuse albedo for these objects is consistent with a value of zero, with a firm upper limit of 10%. Table 2 lists the best-fit specular albedos for the six droplets, which scatter considerably over the range $0.850 \leq A_S \leq 0.993$. Some of this scatter is due to photometric measurement errors, but some of the scatter is also due to uncertainties in the radar-derived diameters used in the best-fit analysis [18]. In particular, the albedo derived for SSN 26521, $A_S = 99.3\%$, appears to be spuriously high. This suggests that the radar-derived diameter [18] of $D = 4.9 \pm 0.2$ cm is too small by $\approx$0.3 cm. Excluding this apparently spurious point, the weighted average of the remaining five derived I-band albedos is $A_S = 0.87 \pm 0.03$. This is within measurement uncertainty of previous measurements of NaK droplet reflectivities in the 480–700 nm V-band [16].

Table 2 indicates that modeling the NaK droplets as purely specular spheres each with its own best-fit albedo generally reproduces the observed I-band brightnesses to within $\approx$0.1 magnitudes. Using an albedo of $A_S = 0.87$ for all of the spheres reproduces the measurements to within $\approx$0.15 magnitudes at the 90% level. This confirms earlier suggestions that the NaK droplets can serve as reasonably high-quality optical calibrators [18].

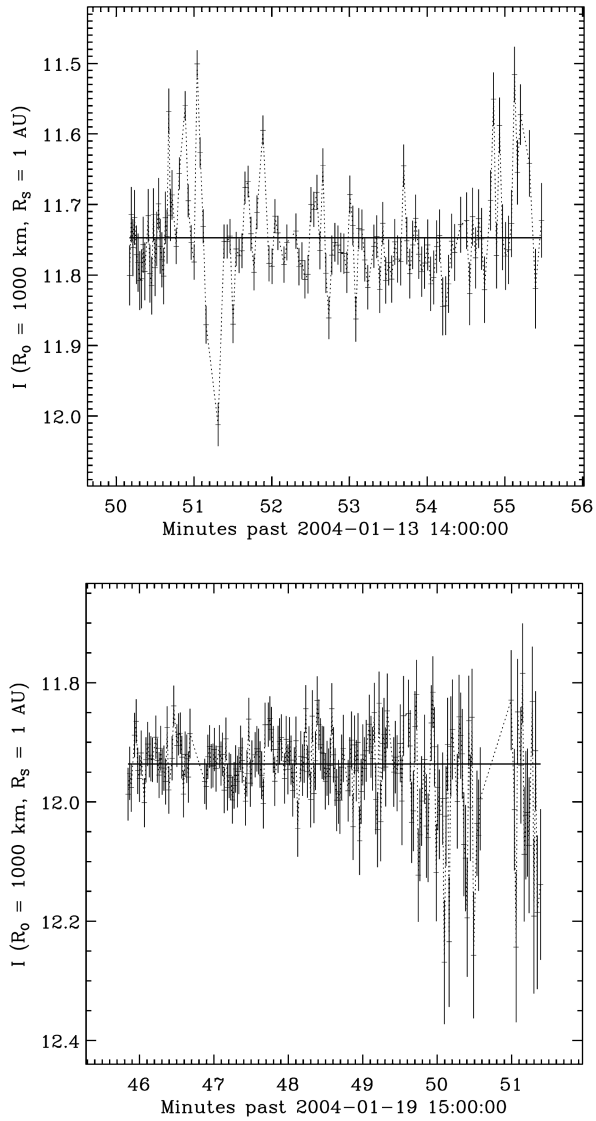

Fig. 8 Range-normalized I-band magnitudes for NaK droplets SSN 26505 and 26521 (+ with error bars connected with dashed lines). The solid lines in both panels show the best-fit specular-sphere models with the albedos given in Table 2.

V. Discussion and Conclusions

The successful development of methods to acquire and process time-resolved I-band photometry from the AMOS 3.6 m AEOS telescope VisIm instrument has enabled the characterization of 12 spherical Earth-orbiting satellites. The calibration procedure relies on observations of photometric standard stars and a least-squares analysis that yields nightly instrumental calibration parameters and atmospheric extinction coefficients. Modeling the 12 observed satellites as uniform spheres reflecting sunlight with specular + diffuse reflectivity components allows least-squares determination of best-fit albedos. The best-fit models provide a means of predicting the brightness of the spheres, facilitating their use as future photometric calibration objects. SSN 01520 appears to be the highest quality calibrator of the 12 spheres investigated, with I-band stellar magnitudes predictable to within $\pm$0.03 at the 90% level. The white paint surface of SSN 01520 also appears to have suffered darkening and become less shiny during several decades of on-orbit space weathering. SSN 01361 appears to be a predominantly specular sphere, consistent with its unpainted aluminum surface. However, SSN 01361 consistently displays systematic $\pm$0.3 magnitude deviations from the uniform-sphere model that recur on a 30–90 s time scale, indicating the existence of optically detectable surface irregularities. Because of this, SSN 01361 can be employed as an optical calibrator only if observations are averaged over much longer periods than the 30–90 s recurrence time scale. Three other radar calibration spheres (SSN 00900, 00902, and 02909) also appear to reflect light in a predominantly specular fashion and occasionally display much larger deviations between measured and model brightnesses. These deviations also likely result from the existence of surface irregularities not captured by the uniform-sphere model. Observations of SSN 04168 confirm that this calibration sphere has a very dark surface with a total albedo of less than 2%, consistent with its known anodized aluminum surface composition. SSN 04168 also possesses at least one optically detectable surface irregularity.

Observations of six NaK droplets confirm that these debris have very nearly spherical shapes and reflect light in a predominantly specular fashion. The measurements are consistent with a diffuse albedo component of zero, with an upper limit of 10%. The average specular albedo of $\approx$87% makes the NaK droplets among the most reflective of all known artificial Earth satellites. Combining this average albedo with diameters estimated from radar observations [18] indicates that the I-band brightness of NaK droplets can be predicted to an accuracy of $\approx$0.15 magnitudes, confirming that these debris can serve as optical calibration objects as well.

Acknowledgment

The authors would like to thank the AEOS telescope operations crew for acquiring the data for this research project.

References

[1] Mayo, J., "AEOS 3.67 Meter Telescope Optics: Design, Fabrication, and Performance," *Proceedings of the 1999 AMOS Technical Conference*, The Maui Economic Development Board, Inc., Kihei, Maui, HI, 1999, pp. 21–32.

[2] Berger, P. J., "AEOS Adaptive Optics System and Visible Imager," *Proceedings of the 1999 AMOS Technical Conference*, The Maui Economic Development Board, Inc., Kihei, Maui, HI, 1999, pp. 47–56.

[3] Roberts, L. C., Jr., and Neyman, C. R., "Characterization of the AEOS Adaptive Optics System," *Publications of the Astronomical Society of the Pacific*, Vol. 114, No. 801, Nov. 2002, pp. 1260–1266.

[4] Landolt, A. U., "UBVRI Photometric Standard Stars in the Magnitude Range $11.5 < V < 16.0$ Around the Celestial Equator," *Astronomical Journal*, Vol. 104, No. 1, July 1992, pp. 340–491.

[5] Wells, D. C., Griesen, E. W., and Harten, R. H., "FITS: A Flexible Image Transport System," *Astronomy and Astrophysics Supplement Series*, Vol. 44, June 1981, pp. 363–370.

[6] Hanisch, R. J., Farris, A., Greisen, E. W., Pence, W. D., Schlesinger, B. M., Teuben, P. J., Thompson, R. W., and Warnock, A., III, "Definition of the Flexible Image Transport System," *Astronomy and Astrophysics*, Vol. 376, Sept. 2001, pp. 359–380.

[7] Howell, S. B., "Introduction to Time-Series Photometry Using Charge-Coupled Devices," *Journal of the American Association of Variable Star Observers*, Vol. 20, No. 2, 1991, pp. 134–149.

[8] Stetson, P. B., "DAOPHOT: A Computer Program for Crowded Field Stellar Photometry," *Publications of the Astronomical Society of the Pacific*, Vol. 99, March 1987, pp. 191–222.

[9] Hardie, R. H., "Photoelectric Reductions," *Astronomical Techniques*, edited by W. A. Hiltner, Univ. of Chicago Press, Chicago, IL, 1962, pp. 157–177.

[10] Lawson, C., and Hanson, R., "Solving Least Squares Problems," Prentice–Hall, Englewood, NJ, 1974.

[11] Livingston, W. C., "Sun," *Allen's Astrophysical Quantities*, edited by A. N. Cox, AIP Press, New York, 1999, pp. 339–380.

[12] Jorgensen, K., Okada, J., Bradford, L., Hall, D., Africano, J., Hamada, K., Sydney, P., Stansbery, G., and Kervin, P., "Obtaining Material Type of Orbiting Objects Through Reflectance Spectroscopy Measurements," *Proceedings of the 2003 AMOS Technical Conference*, The Maui Economic Development Board, Inc., Kihei, Maui, HI, 2003; also Paper 8_SOI-17.

[13] Hall, D., Africano, J., Hamada, K., Kervin, P., Kremeyer, K., Lambert, J., Okada, J., Roberts, L., Jr., and Sydney, P., "AEOS I-Band Photometry of Moving Targets," *Proceedings of the 2003 AMOS Technical Conference*, The Maui Economic Development Board, Inc., Kihei, Maui, HI, 2003; also Paper 8_SOI-11.

[14] King-Hele, D. G., Walker, D. M. C., Pilkington, J. A., Winterbottom, A. N., Hiller, H., and Perry, G. E., *R.A.E. Table of Earth Satellites, 1957–1986*, Stockton Press, New York, 1987.

[15] Kessler, D., Matney, M. J., Reynolds, R. C., Bernhard, R. P., Stansbery, E. G., Johnson, N. L., Potter, A. E., and Anz-Meador, D., "A Search for a Previously Unknown Source of Orbital Debris: The Possibility of a Coolant Leak in Radar Ocean Reconnaissance Satellites," Paper IAA-97-IAA.6.3.03, 1997.

[16] Sridharan, R., Beavers, W., Gaposchkin, E. M., Lambour, R., Kansky, J., and Stansbery, E., "Radar and Optical Characterization of an Anomalous Orbital Debris Population," *Journal of Spacecraft and Rockets*, Vol. 36, No. 5, 1999, pp. 719–725.

[17] Lambour, R., and Sridharan, R., "Characteristics of an Anomalous Orbital Debris Population Inferred from Theoretical Modeling," *Journal of Spacecraft and Rockets*, Vol. 36, No. 5, 1999, pp. 726–735.

[18] Rosenberg, F., "Radar Characterization of RORSAT Coolant Spheres and the Potential Use for Calibration and Validation of Debris Tracking Sensors," MIT LL Project Rept. STK-264, 2003.

[19] Hall, D., Africano, J., Kervin, P., Kelecy, T., Kremeyer, K., Lambert, J., Okada, J., Ross, J., and Sydney, P., "AMOS Measurements of the Physical Properties of NaK Droplets," *Proceedings of the 2004 AMOS Technical Conference*, The Maui Economic Development Board, Inc., Kihei, Maui, HI, 2004, pp. 215–224.

A. Ketsdever
Associate Editor